

Polarization interactions and boroxol ring formation in boron oxide: A molecular dynamics study

Janna K. Maranas^{a)} and Yingzi Chen

Department of Chemical Engineering, The Pennsylvania State University, University Park, Pennsylvania 16802

Dorothea K. Stillinger and Frank H. Stillinger

Lucent Technologies, Murray Hill, New Jersey 07974

(Received 5 February 2001; accepted 18 July 2001)

We employ molecular dynamics (MD) simulations to study the structure of vitreous boron oxide. Although six-membered boroxol rings have been observed at fractions over 60% by various experimental techniques, simulation methods have not produced similar results. We adapt the polarization model, which includes many body polarization effects thought to stabilize such structures, for boron–oxygen interactions. This model is then used in MD simulations of boron oxide glass at various temperatures. We find a variation in the fraction of rings depending on the temperature of the system during network formation. The maximum ring fraction ($\sim 33\%$) occurs when the sample is prepared at low temperatures. At these temperatures, the energy level of boron atoms in rings is 1.6% lower than the energies of boron atoms outside of rings. When higher equilibration temperatures are used, the fraction drops to 11%. Thus, two factors are relevant to boroxol ring formation in simulations of boron oxide, a model which incorporates polarization effects or their equivalent, and the appropriate manipulation of temperature history. © 2001 American Institute of Physics. [DOI: 10.1063/1.1401817]

I. INTRODUCTION

Boron oxide (chemical formula B_2O_3) is a network glass-former. The short-range structure of B_2O_3 is the planar BO_3 triangle, where each boron atom is bonded to three oxygen atoms with O–B–O angles of 120° . The intermediate-range structure, or the arrangement of these triangles, has been established by various experimental techniques as the planar boroxol ring, illustrated in Fig. 1. Boroxol rings at fractions ranging from $f=0.50$ to $f=0.85$ have been observed by inelastic neutron scattering,^{1,2} nuclear magnetic resonance,^{3–6} nuclear quadrupole resonance,^{7–9} Raman scattering,^{10–20} electron paramagnetic resonance^{21,22} and diffraction techniques.^{23,24} Despite the abundant experimental evidence for boroxol rings, the majority of molecular simulation studies do not reveal such structures.^{25–33} A reverse Monte Carlo study³⁴ has shown that a high percentage of boroxol rings cannot reproduce both structural data and density. In one simulation study, a small percentage (approx. 12%) of boroxol rings were observed³⁵ by including polarization of oxygen atoms. The other studies have employed various two-body, three-body, and in one case³³ four-body potentials. In the four-body case, a ring fraction of 3% was observed. One study using a three-body potential³⁶ cites a ring fraction of less than 20%. Another finds 27% of boron atoms in rings, but the resulting density differs from experiment by 10%–37%, depending on the potential.³⁷

Simulation studies thus far have not found experimentally relevant fractions of boroxol rings at reasonable densi-

ties, and the reason for this is uncertain. One suggestion comes from the work of Teter.³⁵ This work used *ab initio* calculations to calibrate a model for boron oxide. These calculations revealed that polarization of the oxygen atoms is crucial in models of this type. Polarization is built into the Teter model by constructing an oxygen ion as a central charge surrounded by four auxiliary charges in tetrahedral symmetry. Within this simple representation of oxygen polarizability, the fraction of boroxol rings increased from less than 1% to a final value of 12% as the magnitude of the auxiliary charges was increased from zero. Thus for a simple ionic model, negligible ring formation was observed, but as polarization effects are introduced, the ring concentration rises.

One of us^{38,39} has developed a more realistic model of polarizability. This model incorporates a many body, nonadditive interaction describing the dipole moments induced by local electric fields. Polarization of oxygen ions thus arises from the other ions present and is dependent upon their locations in the sample and thus its configuration. Potentials for this model have been developed for Si^{4+} , O^{2-} , H^+ , and F^- .⁴⁰ The MD program for this polarization model implements an alternative to periodic boundary conditions that allows for simulation of chemical reactions. Conservative external forces are used to provide what can be viewed as a “chemical reactor containment vessel.” These forces act as semipermeable membranes that selectively pass or block individual atomic species. This allows for a study of reactive processes with automatic removal of reaction by-products. The polarization model has been used to study reactions and charge transfer processes in water^{41–44} and recently has been

^{a)} Author to whom correspondence should be addressed.

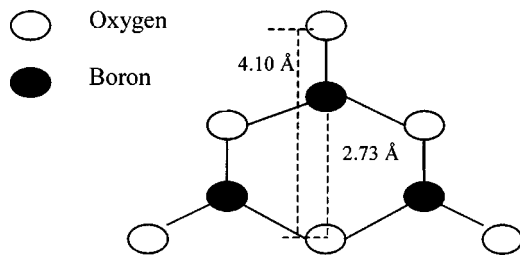


FIG. 1. A schematic illustration of a boroxol ring.

applied to silica glass.⁴⁰ A description of the model is given in Sec. II.

The current paper describes the application of the polarization model to the simulation of vitreous boron oxide. We develop the necessary boron–oxygen and boron–boron potentials by matching structural and energetic data of isolated boron–oxygen and boron–oxygen–hydrogen molecules. This development is presented in Sec. III. We describe in Sec. IV the application of this model to investigate the structure of boron oxide. As with experimental preparation, we begin with an initial system of boric acid [H_3BO_3] molecules, from which dehydration reactions occur, eventually ending with boron oxide [B_2O_3]. The sample is then cooled, and a network structure develops. As expected, the developing structure consists of BO_3 triangles. Whether this network incorporates boroxol rings is sensitive to the temperature at which the system is held during network formation. In the temperature range where boroxol rings are energetically favored, we find a fraction of boroxol rings, $f=0.33$, which, although lower than expected for a vitreous sample at low temperature, is consistent with experimental data in the high temperature end of the glass transition region.

II. POLARIZATION MODEL FORMAT

The task of the polarization model in the present context is to supply a chemically flexible and realistic set of particle interactions to represent the formation and relaxation behavior of boron oxide glasses. More generally, it is required to provide an approximation to Φ , the electronic ground-state potential energy surface for an arbitrary configuration of N atomic particles that may include several elemental species. The mathematical format chosen for the model permits full transferability, provided that the particles remain essentially in the same oxidation (charge) state. In other words, the model is constructed to allow the same set of basic particles to be assembled into a wide variety of molecular or ionic species, and are capable of dynamic chemical interchange between these combinations.

Several previous applications involving polarization model simulations have appeared in print. These include several studies of water cluster structure and reactive dynamics,^{38,42,43,45} a similar study for hydrogen fluoride,⁴⁶ and an examination of phosphoric acid media.⁴⁷ The present work involves an extension and generalization of the previous polarization model version,^{38,39} so for clarity and completeness we now provide a detailed specification of the full

mathematical format used for the boron oxide glass application.

In the following, $\mathbf{r}_1 \cdots \mathbf{r}_N$ will denote the positions of particles $1 \cdots N$ respectively,

$$\mathbf{r}_{ij} = \mathbf{r}_j - \mathbf{r}_i \quad (1)$$

is the vector distance from i to j , and

$$r_{ij} = |\mathbf{r}_{ij}| \quad (2)$$

is the corresponding scalar distance. Each particle i carries an electrostatic charge q_i and has a scalar polarizability α_i ; these remain constant as the N -particle configuration of the system changes. For some species (especially cations) it is expected on physical grounds that the corresponding α_i are negligibly small and can be set equal to zero, but for all others it is positive. If particle i possesses a nonvanishing polarizability, then generally it will exhibit an induced dipole moment $\boldsymbol{\mu}_i$ that represents its response to the presence of other particles and their moments, and that will vary as all particles execute their dynamical motions.

The potential energy function Φ comprises three types of contributions, each dependent on the set of particle positions $\mathbf{r}_1 \cdots \mathbf{r}_N$;

$$\Phi = \Phi_I + \Phi_{II} + \Phi_{III}. \quad (3)$$

The first two of these represent interparticle interactions; the third involves “wall forces” that can selectively confine particles. Both Φ_I and Φ_{II} are chosen to vanish when all N particles are far removed from one another.

Conventional applications of the molecular dynamics simulation technique, and of the related Monte Carlo method,⁴⁸ typically employ periodic boundary conditions to eliminate the presence and influence of surfaces. However the simulation program utilized here takes a different point of view, one in fact that parallels chemical and chemical engineering practice. Conservative external forces are put in place to provide a kind of “chemical reactor vessel.” The external forces can be manipulated so as to act as semipermeable membranes that selectively pass or block individual atomic species. This capacity permits the simulation of chemical reactions with automatic removal of reaction byproducts; specific examples will appear below. Although it plays no role in the present project, the capacity also exists to use appropriate conservative external forces to control the shape of solid samples.

Central pair potentials compose the contribution Φ_I ,

$$\Phi_I = \sum_{i=1}^{N-1} \sum_{j=i+1}^N \phi_{ij}(r_{ij}). \quad (4)$$

Although the subscripts i and j attached to the ϕ 's nominally refer to specific particles, it is only those particles' species that matter in determining which pair function to use; only three distinct species occur in the present application (boron, oxygen, hydrogen). Furthermore, the ϕ 's are invariant to subscript permutation,

$$\phi_{ij}(r_{ij}) = \phi_{ji}(r_{ij}). \quad (5)$$

By themselves, the pair potentials in Φ_I cannot realistically produce polyatomic molecules such as H_2O , B_2O_3 ,

H₃BO₃, etc., with the correct bonding energies and geometries. Inclusion of the many-body interaction Φ_{II} rectifies the situation, however, in particular allowing for the possibility of nonlinear and branched molecules.^{38,47} The structure of Φ_{II} closely parallels that for the classical electrostatic interaction of charged, polarizable point particles, but with short-range modifications that can account for the spatial extension of electron clouds around the nuclei involved.^{38,39} Specifically we have

$$\Phi_{II} = -\frac{1}{2} \sum_{i=1}^N \sum_{j=1, (i \neq j)}^N q_i r_{ij}^{-3} (\mathbf{r}_{ij} \cdot \boldsymbol{\mu}_j) l_{ij}(r_{ij}). \quad (6)$$

In the classical electrostatic precursor, all l 's are identically unity, so in the present polarization model we therefore require

$$\lim_{r \rightarrow \infty} l_{ij}(r) = 1. \quad (7)$$

Furthermore, general considerations require that the l 's should vanish as the cube of r at the origin.^{38,39} Details of chemical bonding behavior place constraints on the forms of these functions at intermediate range (see Sec. II).

In contrast to the ϕ 's, the short-range modification functions l_{ij} generally will not possess subscript interchange symmetry, i.e., $l_{ij}(r)$ may not be the same as $l_{ji}(r)$. As Eq. (6) illustrates, we adhere to the convention that the first subscript (i) refers to a particle whose electrostatic charge is at issue, while the second subscript (j) refers to a particle whose induced moment ($\boldsymbol{\mu}_j$) is required.

Polarization model equations for determining the set of induced moments similarly parallel the classical electrostatic formalism.^{38,39} Once again short-range modification factors (now denoted by k_{ij} 's) are introduced to account for the spatial extent of electron clouds. Consequently the induced dipole vectors have values determined by simultaneous linear relations of the form,

$$\mathbf{R}_i(\boldsymbol{\mu}_1 \cdots \boldsymbol{\mu}_N) = 0 \quad (1 \leq i \leq N), \quad (8)$$

where

$$\mathbf{R}_i = \boldsymbol{\mu}_i + \alpha_i \sum_{j(\neq i)=1}^N r_{ji}^{-3} k_{ji}(r_{ji}) (-q_j \mathbf{r}_{ji} + \boldsymbol{\mu}_j \cdot \mathbf{T}_{ji}). \quad (9)$$

Here $\mathbf{T}_{ji} \equiv \mathbf{T}_{ij}$ is a dyadic tensor,

$$\mathbf{T}_{ji} = \mathbf{1} - 3\mathbf{r}_{ji}\mathbf{r}_{ji}/r_{ji}^2. \quad (10)$$

The k 's obey the analog of Eq. (7),

$$\lim_{r \rightarrow \infty} k_{ij}(r) = 1, \quad (11)$$

and should also vanish cubically at $r=0$.³⁸ As noted for the l_{ij} , subscript order also matters for the k_{ij} .

Finally, Φ_{III} consists of single-particle wall potentials. For the present application we take these to be spherically symmetric about the coordinate origin, and to have a simple power-law character,

$$\Phi_{III} = \varepsilon_{III} \sum_{i=1}^N (r_i/L_i)^p,$$

$$\varepsilon_{III}, L_i, p > 0. \quad (12)$$

The "semipermeable membrane" feature introduced earlier involves assigning different values to the L_i for distinct particle species. Those with small L_i remain confined to a small neighborhood around the origin, while those with large L_i are essentially free to roam over a larger spherical neighborhood. The choice of positive exponent p determines the wall steepness.

Classical molecular dynamics simulation follows the time evolution of an N -body system, utilizing the Newtonian equations of motion,

$$d^2 \mathbf{r}_i / dt^2 = m_i^{-1} \mathbf{F}_i \quad (1 \leq i \leq N) \quad (13)$$

along with suitable initial conditions. Here m_i is the mass of particle i , and \mathbf{F}_i is the total vector force exerted on particle i . In the present context we have

$$\begin{aligned} \mathbf{F}_i &= -\nabla_i(\Phi_I + \Phi_{II} + \Phi_{III}), \\ &\equiv \mathbf{F}_{Ii} + \mathbf{F}_{IIi} + \mathbf{F}_{IIIi}. \end{aligned} \quad (14)$$

Because the forces are conservative, total energy remains constant in time, and the extent to which a numerical integrator for Eq. (13) satisfies this property constitutes a measure of its accuracy. Furthermore, the potential energy Φ as specified above has full rotational symmetry about the coordinate origin, so total angular momentum should also be conserved. This latter attribute would disappear if a different, nonspherical, shape were to be selected for the "walls."

The partial forces \mathbf{F}_{Ii} and \mathbf{F}_{IIIi} have relatively compact expressions when put into explicit form. The former consists of central pair forces exerted on i from all other particles,

$$\mathbf{F}_{Ii} = \sum_{j(\neq i)=1}^N \phi'_{ij}(r_{ij}) (\mathbf{r}_{ij}/r_{ij}). \quad (15)$$

The latter is directed radially inward toward the origin,

$$\mathbf{F}_{IIIi} = -p \varepsilon_{III} L_i^{-p} r_i^{p-2} \mathbf{r}_i. \quad (16)$$

Obtaining explicit expressions for the \mathbf{F}_{IIi} is less straightforward. One reason concerns the fact that the induced moments all depend upon the positions of every particle i . The chain rule for differentiation would seem to imply that operating on Φ_{II} with the gradient ∇_i requires finding the corresponding gradients of induced moment components. However, a simple transformation eliminates this complication. The polarization potential Φ_{II} can formally be augmented by an arbitrary linear combination of the vectors \mathbf{R}_j , Eq. (8), to yield the function

$$\Psi_{II} = \Phi_{II} + \frac{1}{2} \sum_{j=1}^N \alpha_j^{-1} \boldsymbol{\nu}_j \cdot \mathbf{R}_j(\boldsymbol{\mu}_1 \cdots \boldsymbol{\mu}_N) \quad (17)$$

(the linear combination coefficients are written as $\frac{1}{2}\alpha_j^{-1}\boldsymbol{\nu}_j$ for later convenience). Because all \mathbf{R}_j vanish when the correct $\boldsymbol{\mu}$'s are inserted as their arguments, Ψ_{II} and Φ_{II} are equal, and so we can write

$$\mathbf{F}_{IIi} = -\nabla_i \Psi_{II}. \quad (18)$$

The advantage offered by expression Eq. (17) for Ψ_{II} is that the $\boldsymbol{\nu}_j$ can be chosen so that the first variations of Ψ_{II}

with respect to any μ_j all vanish. Hence these induced moments can be treated as constants (rather than as functions of particle positions) for the purposes of calculating the gradient in Eq. (18). Requiring that the first variations vanish leads to a set of equations linear in the ν 's,

$$\mathbf{S}_i(\nu_1 \cdots \nu_N) = 0 \quad (1 \leq i \leq N), \quad (19)$$

where

$$\mathbf{S}_i = \nu_i + \alpha_i \sum_{j(\neq i)=1}^N r_{ij}^{-3} [-q \mathbf{r}_{ji} l_{ji}(r_{ji}) + \nu_j \cdot \mathbf{T}_{ji} k_{ij}(r_{ji})]. \quad (20)$$

The similarity between this set of equations for the ν_j and the prior set Eqs. (8)–(9) for the μ_j is inescapable, and invites naming these ν 's “pseudodipoles.” But notice that the \mathbf{S}_i differ from the \mathbf{R}_i by (a) replacement of k_{ji} by l_{ji} in the sum over charges, and (b) subscript reordering (from k_{ji} to k_{ij}) in the sum over (pseudo) dipoles.

Evaluating the right member of Eq. (18) is straightforward but tedious. The resulting terms can be collected in the following way:

$$\mathbf{F}_{ii} = \sum_{j(\neq i)=1}^N [\mathbf{F}_{ij}^{(q\mu)} + \mathbf{F}_{ij}^{(q\nu)} + \mathbf{F}_{ij}^{(\mu\nu)}]. \quad (21)$$

Notice that each of these contributions to the force on particle i has formally been identified with a specific other particle j . Superscripts $(q\mu)$, $(q\nu)$, and $(\mu\nu)$ for each of these “pair” terms refer, respectively, to interactions between a charge and a dipole, a charge and a pseudodipole, and a dipole and a pseudodipole. We find that the first of these appears as follows:

$$\begin{aligned} \mathbf{F}_{ij}^{(q\mu)} = & \frac{3}{2} r_{ij}^{-5} \mathbf{r}_{ij} [q_i(\mathbf{r}_{ij} \cdot \boldsymbol{\mu}_j) l_{ij}(r_{ij}) - q_j(\mathbf{r}_{ij} \cdot \boldsymbol{\mu}_i) l_{ji}(r_{ij})] \\ & - \frac{1}{2} r_{ij}^{-3} [q_i \boldsymbol{\mu}_j l_{ij}(r_{ij}) - q_j \boldsymbol{\mu}_i l_{ji}(r_{ij})] - \frac{1}{2} r_{ij}^{-4} \mathbf{r}_{ij} [q_i(\mathbf{r}_{ij} \\ & \cdot \boldsymbol{\mu}_j) l'_{ij}(r_{ij}) - q_j(\mathbf{r}_{ij} \cdot \boldsymbol{\mu}_i) l'_{ji}(r_{ij})]. \end{aligned} \quad (22)$$

The second type has a similar form, except that ν 's replace μ 's, and k 's replace l 's,

$$\begin{aligned} \mathbf{F}_{ij}^{(q\nu)} = & \frac{3}{2} r_{ij}^{-5} \mathbf{r}_{ij} [q_i(\mathbf{r}_{ij} \cdot \boldsymbol{\nu}_j) k_{ij}(r_{ij}) - q_j(\mathbf{r}_{ij} \cdot \boldsymbol{\nu}_i) k_{ji}(r_{ij})] \\ & - \frac{1}{2} r_{ij}^{-3} [q_i \boldsymbol{\nu}_j k_{ij}(r_{ij}) - q_j \boldsymbol{\nu}_i k_{ji}(r_{ij})] \\ & - \frac{1}{2} r_{ij}^{-4} \mathbf{r}_{ij} [q_i(\mathbf{r}_{ij} \cdot \boldsymbol{\nu}_j) k'_{ij}(r_{ij}) - q_j(\mathbf{r}_{ij} \cdot \boldsymbol{\nu}_i) k'_{ji}(r_{ij})]. \end{aligned} \quad (23)$$

The third kind of pair contribution in Eq. (21) is the following:

$$\begin{aligned} \mathbf{F}_{ij}^{(\mu\nu)} = & -\frac{3}{2} r_{ij}^{-5} \mathbf{r}_{ij} [(\boldsymbol{\mu}_i \cdot \mathbf{T}_{ij} \cdot \boldsymbol{\nu}_j) k_{ij}(r_{ij}) + (\boldsymbol{\mu}_j \cdot \mathbf{T}_{ji} \cdot \boldsymbol{\nu}_i) k_{ji}(r_{ij})] \\ & + \frac{1}{2} r_{ij}^{-4} \mathbf{r}_{ij} [(\boldsymbol{\mu}_i \cdot \mathbf{T}_{ij} \cdot \boldsymbol{\nu}_j) k'_{ij}(r_{ij}) + (\boldsymbol{\mu}_j \cdot \mathbf{T}_{ji} \cdot \boldsymbol{\nu}_i) k'_{ji}(r_{ij})] \\ & - \frac{1}{2} r_{ij}^{-3} [(\boldsymbol{\mu}_i \cdot \mathbf{t}_{ijx} \cdot \boldsymbol{\nu}_j) \mathbf{u}_x + (\boldsymbol{\mu}_i \cdot \mathbf{t}_{ijy} \cdot \boldsymbol{\nu}_j) \\ & + (\boldsymbol{\mu}_i \cdot \mathbf{t}_{ijz} \cdot \boldsymbol{\nu}_j) \mathbf{u}_z] k_{ij}(r_{ij}) - \frac{1}{2} r_{ij}^{-3} [(\boldsymbol{\mu}_j \cdot \mathbf{t}_{ijx} \cdot \boldsymbol{\nu}_i) \mathbf{u}_x \\ & + (\boldsymbol{\mu}_j \cdot \mathbf{t}_{ijy} \cdot \boldsymbol{\nu}_i) \mathbf{u}_y + (\boldsymbol{\mu}_j \cdot \mathbf{t}_{ijz} \cdot \boldsymbol{\nu}_i) \mathbf{u}_z] k_{ji}(r_{ij}). \end{aligned} \quad (24)$$

The last part of this expression has been displayed explicitly as separate Cartesian components, with unit vectors along the x , y , and z directions denoted by \mathbf{u}_x , \mathbf{u}_y , and \mathbf{u}_z , respec-

TABLE I. Fundamental properties of species. The polarizability for oxygen was obtained from Ref. 38.

Species	q_i/e	α_i (\AA^3)	m_i/m_H
B	+3	0.0000	11
O	-2	1.444	16
H	+1	0.0000	1

tively. The 3×3 \mathbf{t} matrices have forms that appear in Appendix A. This completes the specification of the forces needed to integrate the Newtonian equations of motion.

In order to facilitate chemical interpretation of the N -particle configurations encountered during the molecular dynamics simulations, it is useful to introduce a geometric convention for the presence of chemical bonds in the system. The two types of bonds expected in the present context are those involving a pair of particles bearing opposite charges, namely OH, and OB. For the purposes of bond enumeration and of graphical presentation we define a bond to exist if the corresponding pair distance is less than 1.2 \AA for OH, and less than 1.55 \AA for OB. The reader should note that these cutoff distances substantially exceed equilibrium bond lengths so as to count interactions that may have temporarily experienced significant vibrational stretching.

In addition to bond enumeration, the system configurations generated by solving the Newtonian dynamical equations lead to “inherent structures” (local Φ minima) by means of a steepest-descent mapping on the Φ hypersurface.^{49,50} These inherent structures are mechanically stable arrangements of the N particles in space, and by construction are free from vibrational deformation. The force expressions presented in this section are required in order to carry out the mapping of dynamical configurations to inherent structures. A significant advantage of the inherent structures over the dynamical configurations that spawn them is their lesser sensitivity to the arbitrarily-chosen bond cutoffs in bond enumeration.⁵¹

III. DEVELOPMENT OF INPUT FUNCTIONS FOR B^{3+}

For the simulations presented here, we require potentials to describe all interactions between H^+ , O^{2-} , and B^{3+} . Table I shows the charges, polarizabilities, and masses assigned to these species. The masses correspond to the most abundant naturally occurring isotope. The hydrogen ion is a bare proton, and thus assigning it a vanishing polarizability is natural. The boron cation carries two electrons, which are tightly bound. Hence, we have also taken the polarizability of B^{3+} as zero.

The pairwise potentials, $\phi_{ij}(r)$ are required for all pairs, and the short-range modification functions $k_{ij}(r)$ and $l_{ij}(r)$ are required when j has a nonzero polarizability. The following potential functions have been previously developed⁴⁰ and are given in Appendix B: $\phi_{OO}(r)$, $\phi_{HO}(r)$, $k_{OO}(r)$, $k_{HO}(r)$, $l_{OO}(r)$, and $l_{HO}(r)$. The units used there and in the results to follow are kcal/mol for energy and \AA for length. The fundamental proton charge in these units is $e = (332.1669 \text{\AA} \text{ kcal/mol})^{1/2}$. This section describes the development and subsequent testing of the remaining input func-

tions: $\phi_{\text{BB}}(r)$, $\phi_{\text{BO}}(r)$, $\phi_{\text{BH}}(r)$, $k_{\text{BO}}(r)$, and $l_{\text{BO}}(r)$. The strategy we employ for assignment of the functions is to optimize the fitting of properties of isolated molecules. We have used structural data (bond lengths, bond angles) for BO^+ ,⁵² HBO_2 ,^{53–55} B_2O_3 ,^{53,54,56,57} H_3BO_3 ,^{58,59,60} and the dipole moment, dipole derivative, and harmonic force constant for BO^+ .⁵² The structures resulting from the model potentials were assessed by use of the MINOP procedure to determine the minimum energy structure.

A. Pairwise potentials

The pair interactions are dominated at large distances by the Coulomb interaction between appropriate charges,

$$\phi_{ij}(r) \rightarrow \frac{q_i q_j}{r}. \quad (25)$$

At short separations, these functions diverge to infinity due to repulsion. For pairs of species where chemical bond formation is possible, this function should have a minimum at or near the equilibrium bond length. The starting point for assignment of pair potential functions are these limiting features.

The boron–boron interaction is left as

$$\phi_{\text{BB}}(r) = \frac{9e^2}{r}. \quad (26)$$

However, the boron–hydrogen interaction required modification to increase the repulsion at small distances. Without this modification the H–O–B angle in HBO_2 was much smaller than available experimental data suggests is appropriate.⁵⁵ The final form

$$\phi_{\text{BH}} = \frac{3e^2}{r} + 500 \exp(-0.8r) \quad (27)$$

represents a compromise between known H–O–B angles in HBO_2 and H_3BO_3 .

In the oxygen–boron interaction, there must be a modification that reflects the potential for chemical bonding. In assigning the modification we use the following conditions for the BO^+ molecule:

$$\begin{aligned} \Phi'(r_e) &= 0, \\ \Phi''(r_e) &= k. \end{aligned} \quad (28)$$

The first condition reflects the fact that the total potential must have a minimum at the equilibrium bond length, and the second represents force constant for that value. The value of the harmonic force constant for BO^+ was obtained from Peterson,⁵² and a value of $r_e = 1.175 \text{ \AA}$ was used for the equilibrium bond length. The resulting pairwise interaction function,

$$\begin{aligned} \phi_{\text{BO}}(r) &= \frac{-6e^2}{r} + \frac{667.1268}{r^4} - 1597.408652(r - r_3)^2 \\ &\times \exp[-25(r - r_e)^2] \end{aligned} \quad (29)$$

is shown in Fig. 2.

The oxygen–oxygen pairwise interaction function also required modification from its original form⁴⁰ because the

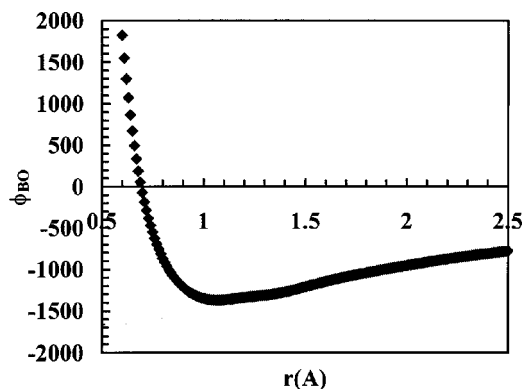


FIG. 2. The boron–oxygen pair potential, $\phi_{\text{BO}}(r)$.

energy at the O–O separation distance relevant to a boron atom bonded to three oxygens was large enough to prevent threefold coordinated boron atoms. The O–O repulsion was lessened by an amount that results in a B–O bond distance in threefold coordinated molecules which is as close as possible to known values⁶¹ (approx. 1.37 \AA). We also required that the geometry of the water dimer (which was used to make the initial assignment) was changed as little as possible. This modified function is given in Appendix B.

B. Polarization functions

The polarization functions have been assigned with the limiting values in Sec. II, namely, that both l_{BO} and k_{BO} approach unity at large distances and vanish cubically at $r = 0$. For k_{BO} , we consider the dipole moment of BO^+ ,

$$\mu_{\text{BO}^+} = \frac{-3ek_{\text{BO}}(r_e)}{r_e^2}. \quad (30)$$

Numerical values for the dipole moment and dipole derivative⁵² were used to assign the function,

$$\begin{aligned} k_{\text{BO}}(r) &= 0.023809r^3 + 0.375294r^6 - 0.0971471r^9 \\ &r \leq r_e, \\ k_{\text{BO}}(r) &= 1 - [0.388471 + 1.96519(r - r_e)] \\ &\times \exp[-10.1175(r - r_e)] \quad r > r_e. \end{aligned} \quad (31)$$

We choose l_{BO} such that the total energy of the B_2O_3 molecule has a minimum at the B–O–B angle for which there is the most evidence, $\theta = 137^\circ$,^{56,57}

$$l_{\text{BO}}(r) = 1 - [1 + 1.552r + 1.204352r^3] \exp(-1.552r). \quad (32)$$

Both the k and l functions for BO interactions are plotted in Fig. 3.

C. Verification of function choices

The function choices outlined above were confirmed by comparisons of model-generated minimum energy structures with experimental and *ab initio* structures for B_2O_3 , HBO_2 , and H_3BO_3 , as discussed above, and for $\text{H}_3\text{B}_3\text{O}_6$ (Refs. 59, 60) and $\text{H}_4\text{B}_2\text{O}_5$.⁵⁹ Results for B_2O_3 , H_3BO_3 , and HBO_2 are shown in Fig. 4. In all cases, the lengths of double and

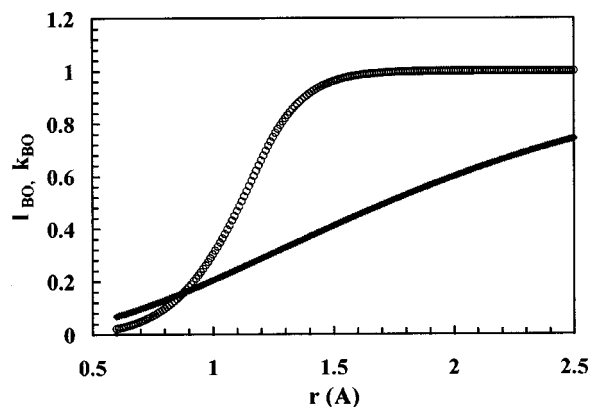


FIG. 3. Polarization functions for boron–oxygen interactions. Solid symbols, $I_{BO}(r)$; open symbols, $k_{BO}(r)$.

single B–O bonds are higher than comparable data suggests. However, we have preserved the difference between the double and single bond lengths of approximately 0.1 Å. The single B–O bond also increases in going from twofold to threefold coordination, in agreement with available structural data. A comparison of relative energy values between molecules is given in Table II. This also indicates reasonable agreement with available data.

IV. APPLICATION TO THE BORON OXIDE STRUCTURE

The polarization model with the function assignments described in Sec. III was used to carry out molecular dynamics calculations as described in Sec. II. The initial system consisted of 81 boric acid [H_3BO_3] molecules arranged in a regular array of approximately $10 \times 10 \times 16$ Å. The molecules are spaced by 5 Å along the two directions parallel to the plane of the molecule and 2 Å perpendicular to this plane. This selection of initial system allows us to closely follow the normal experimental preparation method for boron oxide glass, namely dehydration of boric acid. All particle velocities were initially set to zero. In all simulations described here, a time step of 0.2 fs was used. The wall parameters in Φ_{III} [Eq. (12)] were chosen as

$$L_O = L_H = 40.0 \text{ \AA},$$

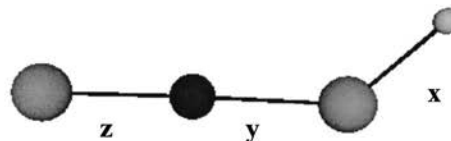
$$L_B = 20.0 \text{ \AA}.$$

These selections were made so that as water molecules are formed via dehydration reactions, they are free to leave the “reaction zone,” while species containing boron remain. As the Gear algorithm began to advance the system in time, the boric acid molecules quickly decomposed, primarily through the following reactions:

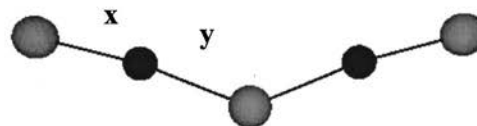


As these reactions are highly exothermic, the temperature of the system rose strongly and velocity scaling between runs was used to keep the temperature in the neighborhood of 6000 K. As the simulation proceeded, water molecules accumulated outside of the reaction zone. These molecules interact only weakly with the inner core, however their presence

(a) Property	Polarization Model	Experiment
$x(\text{\AA})$	1.07	0.9611
$y(\text{\AA})$	1.35	1.33
$z(\text{\AA})$	1.27	1.22
$\Theta_{HOB}(\text{deg})$	118.32	125.7



(b) Property	Polarization Model	Experiment
$x(\text{\AA})$	1.26	1.20
$y(\text{\AA})$	1.36	1.33
$\Theta_{BOB}(\text{deg})$	136	137



(c) Property	Polarization Model	Experiment
$x(\text{\AA})$	1.038	0.900
$y(\text{\AA})$	1.416	1.362

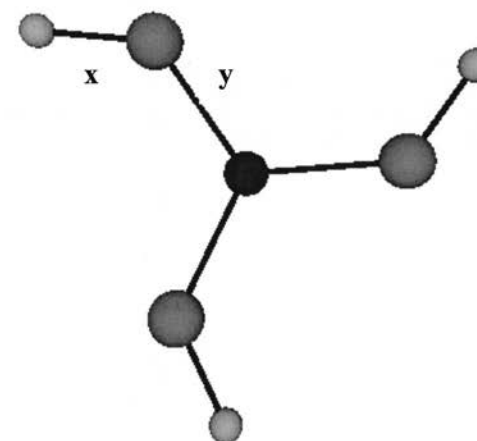


FIG. 4. Structural properties of isolated molecules. (a) HBO_2 ; (b) B_2O_3 ; (c) H_3BO_3 .

TABLE II. Energies of molecules relative to H_3BO_3 from the polarization model and *ab initio* calculations.

Energy	Polarization model	Reference 59	Reference 60
$\Phi(H_3B_3O_6)/\Phi(H_3BO_3)$	2.19	2.12	2.027
$\Phi(H_4B_2O_5)/\Phi(H_3BO_3)$	1.716	1.675	...

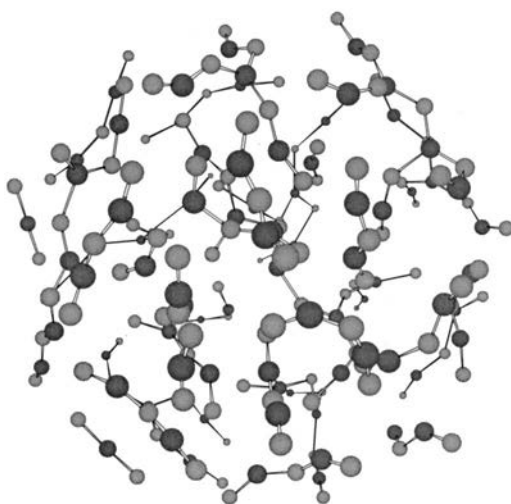


FIG. 5. The boron–oxygen system at 3440 K. The dark atoms are B^{3+} and the light are O^{2-} . A boron–oxygen bond is drawn if the separation is less than 1.55 Å.

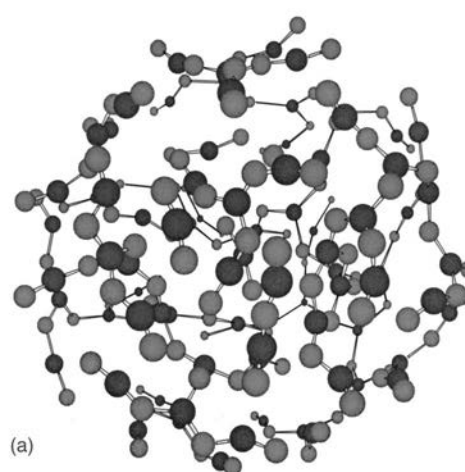
places computational demands on the molecular dynamics simulation program. For this reason, the simulation was periodically stopped for removal of these molecules from the system. Other reactions occurred to a minor extent, resulting in the formation of a few OH^- groups. These were removed from the outer zone with the water molecules. As the dehydration reactions proceeded, the L parameter for boron was decreased to

$$L_B = 8 \text{ \AA}$$

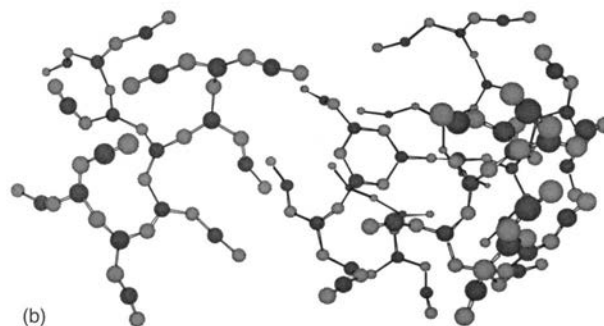
in stages.

After 64 ps at these conditions, no hydrogen remained in the system, which consisted of the 81 boron atoms in the system initially, and 124 oxygen atoms; primarily in the form of B_2O_3 molecules. If the system were macroscopic, a few H_2O s might have remained trapped. At this point, some linkages between molecules had formed and a few BO_3 triangles were present in the system. At this point, we began cooling the system from the relatively high temperature (6000 K) used to facilitate dehydration. In this stage, the L parameters were chosen so that the experimentally relevant density (1.84 g/cm^3) was maintained in the sample. This was chosen by determining the moment of inertia of the sample and equating it to a hypothetical sphere of radius r and density 1.84 g/cm^3 . The resulting radius was used to set the common L parameter for boron and oxygen. It was then adjusted as necessary during the course of the remaining simulations to maintain the proper density.

As the temperature was lowered in stages, the molecules began to arrange themselves in a network formation comprised of BO_3 triangles. Figure 5 illustrates the extent of network formation at a temperature of approximately 3500 K. As the temperature was lowered further and network formation continued, two alternate procedures were used. In procedure 1, the temperature was held at approximately 2000 K until most of the network had formed (128 ps). The temperature was then lowered again in stages, but at much lower cooling rate, to a final temperature of 1700 K. In this sample, one boroxol ring is present in the final structure shown in



(a)



(b)

FIG. 6. (a) The boron–oxygen system formed at high temperature. The dark atoms are B^{3+} and the light are O^{2-} . A boron–oxygen bond is drawn if the separation is less than 1.55 Å. (b) The same system as (a) with the large sections spatially separated so their structure may be more easily seen.

Fig. 6, although it did break up and reform during the course of the simulation. In procedure 2, the temperature was held at approximately 1800 K while network formation was completed, and then cooled in stages until it reached 700 K. The final structure of this sample as illustrated in Fig. 7 is markedly different, with four planar boroxol rings and one eight-membered ring. Of the boron atoms in the network structure with threefold coordination, this amounts to 33% in boroxol rings. This value is consistent with experimental estimates of the fraction of boroxol rings [approximately 32% at 1000 K (Ref. 17)].

To ensure that the density of the subsystem consisting of threefold coordinated boron atoms is equivalent to that of the sample as a whole, we calculated the density of a sphere centered at the origin, but extending to only 6.5 Å rather than the 8.5 Å radius of the entire system. The 6.5 Å sphere contains 20 threefold coordinated and 5 twofold coordinated boron atoms, while the entire sphere contains 36 threefold coordinated and 45 twofold coordinated boron atoms. If the densities of three fold and twofold coordinated subsystems differ substantially, this will show up as a difference in the densities of the 6.5 and 8.5 Å spheres. The calculations yield 1.84 g/cm^3 for the density of the whole system and 1.83 g/cm^3 for the density of the 6.5 Å system. This leads to densities of 1.824 and 1.852 g/cm^3 for threefold and twofold coordinated atoms, respectively. This is a deviation of less than one percent from the experimental density.

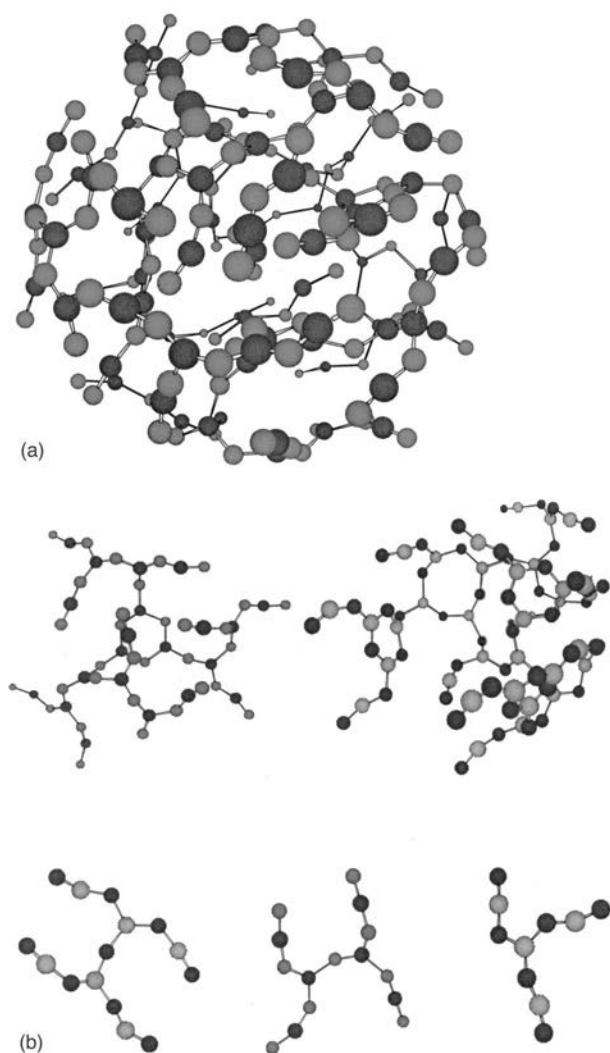


FIG. 7. (a) The system formed at low temperature. The dark atoms are B^{3+} and the light are O^{2-} . A boron–oxygen bond is drawn if the separation is less than 1.55 \AA . (b) The same as (a) with large clusters spatially separated so their structure may be more easily seen. Four boroxol rings and one eight-membered ring are present. This amounts to 44% of boron atoms in ring structures.

To explain our observations, we have calculated the energies of ring versus nonring threefold coordinated boron atoms at 1831 K and at 1967 K. These calculations are summarized in Table III. We use only Φ_I and Φ_{II} in determining these energies, as Φ_{III} reflects the proximity of the structure in question to the hypothetical spherical container. Since the ring structures are located primarily in the interior of the system, including the wall energy would unfairly bias the

TABLE III. Energies of boroxol ring formation. All energies are in kcal/mol.

Potential	$T=1830 \text{ K}$		$T=1967 \text{ K}$	
	Rings	Nonrings	Rings	Nonrings
Φ_I	-1885.54	-1894.45	-1888.06	-1897.6
Φ_{II}	-189.68	-147.15	-168.4	-154.4
$\Phi_I + \Phi_{II}$	-2075.22	-2041.6	-2056.46	-2052.01

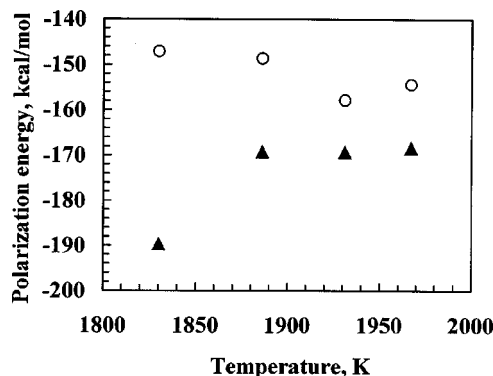


FIG. 8. Energies calculated from the polarization potential as a function of temperature. Open symbols: boron atoms in nonring structures. Closed symbols: boron atoms in ring structures.

results. These calculations show that ring structures are energetically favored at 1831 K by 1.6%, while at 1967 K, there is little difference. The difference in energies for the ring versus non-ring structures arises primarily from the polarization part of the potential (Φ_{II}). The energies calculated from this potential are plotted as a function of temperature in Fig. 8. We have only included calculations for temperatures where we feel sufficient time for equilibration has elapsed. It is apparent from the figure that the polarization energy strongly favors ring structures as the temperature is decreased. This suggests that holding the system at high temperatures where ring formation is not energetically favored as network formation occurs prevents the formation of boroxol rings. Ring formation does not occur, even if the system is subsequently cooled into the range where it is favored, perhaps because of an energy barrier or kinetic limitations for the transformation within the network. This has obvious implications for simulation work, where high temperatures are often used for equilibration. It should be noted that surface effects likely play a large role in our simulations, as a network cluster as small as the one studied here must be dominated by surface effects. Since the rings in our cluster are all located in the interior, it is likely that a cluster absent of surface effects would have larger ring concentration.

The pair distribution functions for the high temperature (no rings) and low temperature structures are compared in Fig. 9. The O–O, O–B, and B–B correlations are shown. Differences resulting from the presence of rings are minor. Both the O–O and O–B distributions have an additional small peak when rings are present. In the O–B distribution, this peak appears at 2.8 \AA , the position of the nearest O–B separation in a ring (see Fig. 1). In the O–O distribution, this peak appears at 4.2 \AA , the next nearest O–O separation in a ring (see Fig. 1).

Figure 10 shows the average energy obtained from the simulation runs as a function of the average temperature. Also shown in the figure are the energies of the “inherent structures,” obtained by subjecting the final system configuration in each run to the MINOP procedure. There are no obvious differences in the two configurations. At high temperatures, the energies are relatively insensitive to temperature, but in the range 3000–1500 K, the energies change

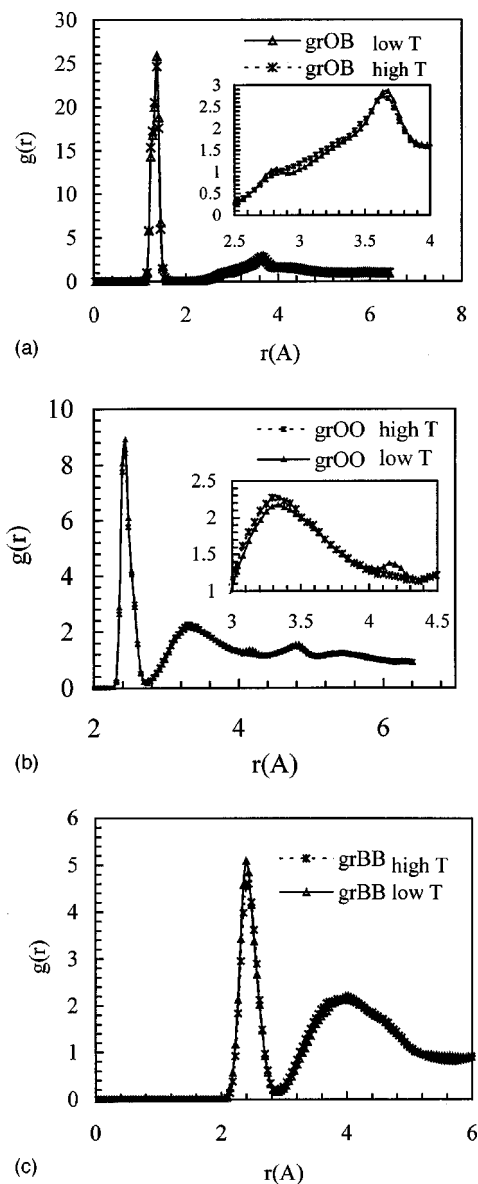


FIG. 9. (a) The boron–oxygen pair distribution function for low temperature (boroxol ring formation) and high temperature (no ring formation) preparations. The inset is a blowup of the region where small differences due to ring formation appear. (b) The oxygen–oxygen pair distribution function for low temperature (boroxol ring formation) and high temperature (no ring formation) preparations. The inset is a blowup of the region where small differences due to ring formation appear. (c) The boron–boron pair distribution function for low temperature (boroxol ring formation) and high temperature (no ring formation) preparations.

more rapidly with temperature, eventually reaching a low temperature plateau. It should be noted that the low temperature runs are most likely not equilibrium structures due to time limitations of computer simulations. This type of change in energy is indicative of glass formation, and the small changes observed here are consistent with a strong glass former, as well as with a fast cooling rate.

V. DISCUSSION AND CONCLUDING REMARKS

This study has applied the polarization model to investigate the intermediate-range structure in boron oxide, a network glass former regarded as strong in the classification

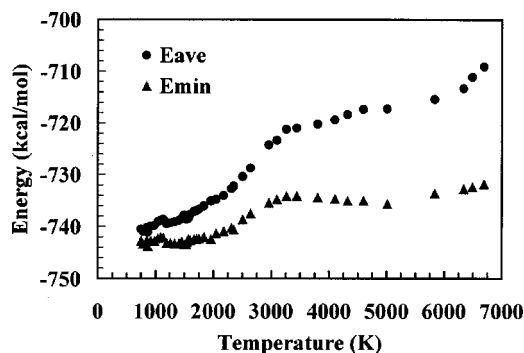


FIG. 10. Potential energy per particle as a function of temperature. Both the average energy from the simulation run, and the inherent structure energy found by minimizing the energy from the ending coordinates are shown.

scheme of Angell. This model allows for polarization of oxygen atoms by the surrounding boron atoms, and is thus inherently a many body potential. The selection of input functions to the model was made on the basis of isolated molecules containing boron, oxygen and hydrogen. With these selections, the polarization model predicts structural properties (i.e., bond lengths and angles) within 5% of their known values. Perhaps more importantly than numerical agreement is the agreement of trends within structural features; for example the difference in the B–O bond length between twofold and threefold coordinated boron atoms. One should not expect that any simulation model would perfectly correlate numerical values of experimental observables, but an accurate representation of trends among these observables is a good measure of model performance.

Having set and tested the model input functions, we used the polarization model to investigate the network structure in boron oxide glass. The formation of a trigonal network in boron oxide as the temperature is lowered closely parallels experimental observations of the glass transition. Based on a large number of experimental studies, this network is thought to consist to a large extent of boroxol rings, with the concentration of boron atoms in rings increasing through the transition region. However, the confirmation of large ring fractions with computer simulation has been difficult. We prepared vitreous nanobeads by dehydrating boric acid (a common experimental precursor) and quenching into the region where significant motion is not observed over the time scale of our simulations. The temperature range over which a transition to the vitreous state is observed in these simulations, 1500–3000 K, is displaced significantly from the corresponding range (500–1200 K) of experimental observations. This is expected in light of the extremely short time scales observable via computer simulation (on the order of nanoseconds) and the even shorter time scales accessible in the present simulations (approx 0.3 ns total for the longer low T run). It is likely that the energy drop off in Fig. 10 would continue, were additional computer time available for longer equilibration at the lower temperatures. Simulations of this nature are currently underway. The onset of network formation occurs around 3000 K, i.e., it coincides with the onset of the transition region. As the energy drops through the transition range, network formation becomes more com-

plete. However, even at the lower end of this transition, the system is not fully interconnected.

In these simulations, we observe that the creation of boroxol rings occurs at the time of network formation. Boroxol rings form at temperatures less than about 2000 K, about 1000 K lower than the onset of network formation. An energy analysis shows that ring structures are favored at temperatures lower than this cutoff. If the system is held above 2000 K as network formation proceeds, ring structures are not incorporated in the network structure. Subsequent cooling to temperatures where ring formation is favored does not cause the network in place to rearrange into one which is rich in boroxol rings. In contrast, if the system is held below 2000 K as the network structure forms, a significant fraction of boroxol rings is incorporated. We find that the fraction of boron atoms in planar, six-membered rings is 33% for two average rates of cooling through the region 2500–1700 K. This suggests that the fraction observed at 1700 K is not an artifact of a fast quench, although the continuation of the faster cooling rate to lower temperatures likely arrests further ring formation. In addition to containing a significant fraction of planar boroxol rings, the density of our simulated system differs from the experimental density by less than 1%. The fact that the network is not completely interconnected supports the theory of Wright *et al.*⁶² that models for boron oxide can satisfy the experimental density and have large boroxol rings fractions if they contain locally independent interpenetrating networks. The ring fraction of 33% corresponds to that observed experimentally at approximately one-third of the temperature interval preceding the glass transition, i.e., at a temperature around 1000 K. We are currently continuing the simulations at lower temperatures with longer equilibration times to test for additional ring formation.

We have calculated the pair distribution functions of the various types of atoms in the simulation: O–O, B–B, and

O–B, for the system with significant ring formation (33% of boron atoms in planar boroxol rings), and no ring formation. The differences in the distributions are minor, with small features appearing in the O–O and O–B distributions that correspond to the cross-ring distances in boroxol rings. These minor differences may be difficult to detect in x-ray diffraction measurements, where the O–O and O–B distributions are smeared together. Evidently, the preferred separation distances in boron oxide networks can be satisfied by both ring and nonring configurations.

We close with a comment on the cause of significant boroxol ring formation in our simulations. We have not used any explicit three-body or four-body potentials in these simulations, rather we have employed a model that includes the effect of oxygen polarization, developed to describe isolated molecules. It is tempting to attribute the observation of significant ring formation to the level of realism in the model. However, ring formation is obviously sensitive to temperature. Therefore, one cannot exclude the possibility that the temperature at which network formation occurs is the primary contributor to ring formation. In other words, a simulation done with a model that neglects polarization, yet carries out network formation in the temperature range where ring structures are favored may result in significant ring formation. This would seem to be the case in the simulations of Youngman³⁶ and Takada.³⁷ However, we find that the energy stabilization of ring versus nonring structures originates from the polarization part of the potential. Further, the simulations of Teter³⁵ clearly show that the fraction of boroxol rings is related to the extent of polarization of oxygen atoms.

ACKNOWLEDGMENT

This work was supported by the National Science Foundation, Division of Materials Research, Materials Theory Program, under Grant No. DMR-0074714.

APPENDIX A

Equation (24) contains a set of 3×3 matrices that have the following explicit forms:

$$t_{ijx} = t_{jix} = -3 \begin{bmatrix} -\frac{2x_{ij}}{r_{ij}} + \frac{2x_{ij}^3}{r_{ij}^4} & -\frac{y_{ij}}{r_{ij}^2} + \frac{2x_{ij}^2 y_{ij}}{r_{ij}^4} & -\frac{z_{ij}}{r_{ij}^2} + \frac{2x_{ij}^2 z_{ij}}{r_{ij}^4} \\ -\frac{y_{ij}}{r_{ij}^2} + \frac{2x_{ij}^2 y_{ij}}{r_{ij}^4} & \frac{2x_{ij} y_{ij}^2}{r_{ij}^4} & \frac{2x_{ij} y_{ij} z_{ij}}{r_{ij}^4} \\ -\frac{z_{ij}}{r_{ij}^2} + \frac{2x_{ij}^2 z_{ij}}{r_{ij}^4} & \frac{2x_{ij} y_{ij} z_{ij}}{r_{ij}^4} & \frac{2x_{ij} z_{ij}^2}{r_{ij}^4} \end{bmatrix}; \quad (\text{A1})$$

$$t_{ijy} = t_{jiy} = -3 \begin{bmatrix} \frac{2x_{ij}^2 y_{ij}}{r_{ij}^4} & -\frac{x_{ij}}{r_{ij}^2} + \frac{2x_{ij} y_{ij}^2}{r_{ij}^4} & \frac{2x_{ij} y_{ij} z_{ij}}{r_{ij}^4} \\ -\frac{x_{ij}}{r_{ij}^2} + \frac{2x_{ij} y_{ij}^2}{r_{ij}^4} & -\frac{2y_{ij}}{r_{ij}^2} + \frac{2y_{ij}^3}{r_{ij}^4} & -\frac{z_{ij}}{r_{ij}^2} + \frac{2y_{ij}^2 z_{ij}}{r_{ij}^4} \\ \frac{2x_{ij} y_{ij} z_{ij}}{r_{ij}^4} & -\frac{z_{ij}}{r_{ij}^2} + \frac{2y_{ij}^2 z_{ij}}{r_{ij}^4} & \frac{2y_{ij} z_{ij}^2}{r_{ij}^4} \end{bmatrix}; \quad (\text{A2})$$

$$t_{ijz} = t_{jiz} = -3 \begin{bmatrix} \frac{2x_{ij}^2 z_{ij}}{r_{ij}^4} & \frac{2x_{ij} y_{ij} z_{ij}}{r_{ij}^4} & -\frac{x_{ij}}{r_{ij}^2} + \frac{2x_{ij} z_{ij}^2}{r_{ij}^4} \\ \frac{2x_{ij} y_{ij} z_{ij}}{r_{ij}^4} & \frac{2y_{ij}^2 z_{ij}}{r_{ij}^4} & -\frac{y_{ij}}{r_{ij}^2} + \frac{2y_{ij} z_{ij}^2}{r_{ij}^4} \\ -\frac{x_{ij}}{r_{ij}^2} + \frac{2x_{ij} z_{ij}^2}{r_{ij}^4} & -\frac{y_{ij}}{r_{ij}^2} + \frac{2y_{ij} z_{ij}^2}{r_{ij}^4} & -\frac{2z_{ij}}{r_{ij}^2} + \frac{2z_{ij}^3}{r_{ij}^4} \end{bmatrix}. \quad (\text{A3})$$

APPENDIX B: OO AND OH FUNCTIONS

1. Pair potentials

$$\phi_{\text{HH}}(r) = \frac{e^2}{r}, \quad (\text{B1})$$

$$\begin{aligned} \phi_{\text{OH}}(r) = & \frac{-2e^2}{r} [1 - 5 \exp(-3.69939282r)] \\ & + [-184.6966743(r - r_0) \\ & + 123.9762188(r - r_0)^2] \exp[-16(r - r_0)^2], \end{aligned} \quad (\text{B2})$$

$$\begin{aligned} \phi_{\text{OO}}^{\text{mod}}(r) = & \frac{4e^2}{r} + 109.6215 \exp[-4.461(r - 2.4)] \\ & + \frac{28.9808}{1 + \exp[2.3667(r - 2.5735)]} \\ & - \frac{156.263}{1 + \exp[8.1395(r - 2.4061)]}. \end{aligned} \quad (\text{B3})$$

2. Polarization functions

$$\begin{aligned} k_{\text{BO}}(r) = & k_{\text{OO}}(r) \\ = & 1.229874160r^6 - 1.055768877r^9 \\ & + 0.2934803065r^{12}; \quad r \leq 0.9584 \\ = & 1 - 0.698298189 \exp[-1.211929802(r \\ & - 0.9584)] + 0.230861592 \exp[-9(r \\ & - 1.25)^2]; \quad r \geq 0.9584. \end{aligned} \quad (\text{B4})$$

¹A. C. Hannon, D. I. Grimley, R. A. Hulme, A. C. Wright, and R. N. Sinclair, *J. Non-Cryst. Solids* **177**, 299 (1994).

²M. Massot, S. Souto, and M. Balkanski, *J. Non-Cryst. Solids* **182**, 49 (1995).

³G. E. Jellison, Jr., L. W. Panek, P. J. Bray, and G. B. Rouse, Jr., *J. Chem. Phys.* **66**, 802 (1977).

⁴G. E. Jellison and P. J. Bray, *J. Non-Cryst. Solids* **29**, 187 (1978).

⁵R. E. Youngman and J. W. Zwanziger, *J. Non-Cryst. Solids* **168**, 293 (1994).

⁶J. W. Zwanziger, U. Werner-Zwanziger, and C. Joo, *Abstr. Pap.-Am. Chem. Soc.* **218**, 43-GE0C (1999).

⁷S. J. Gravina, P. J. Bray, and G. L. Petersen, *J. Non-Cryst. Solids* **132**, 165 (1990).

⁸P. J. Bray, S. Gravina, and D. Lee, in *Boron-Rich Solids*, edited by D. Emin, T. L. Aselage, and B. Morosin, *AIP Conf. Proc.* **231**, 271 (1991).

⁹P. J. Bray, J. F. Emerson, D. Lee, S. A. Feller, D. L. Bain, and D. A. Feil, *J. Non-Cryst. Solids* **129**, 240 (1991).

¹⁰F. Galeener, G. Lucovsky, and J. C. Mikkelsen, Jr., *Phys. Rev. B* **22**, 3983 (1980).

¹¹F. L. Galeener and A. E. Geissberger, *J. Phys. (Paris), Colloq.* **C9**, 343 (1982).

¹²C. F. Windisch, Jr., and W. M. Risen, Jr., *J. Non-Cryst. Solids* **48**, 307 (1982).

¹³W. M. Risen, Jr., *J. Non-Cryst. Solids* **76**, 97 (1985).

¹⁴C. F. Windisch Jr. and W. M. Risen, Jr., *J. Non-Cryst. Solids* **48**, 325 (1982).

¹⁵G. E. Walrafen, M. S. Hokmabadi, P. N. Krishnan, S. Guha, and R. G. Munro, *J. Chem. Phys.* **79**, 3609 (1983).

¹⁶S. Guha and G. E. Walrafen, *J. Chem. Phys.* **80**, 3807 (1984).

¹⁷A. K. Hassan, L. M. Torell, L. Börjesson, and H. Doweidar, *Phys. Rev. B* **45**, 12797 (1992).

¹⁸F. L. Galeener and M. F. Thorpe, *Phys. Rev. B* **28**, 5802 (1983).

¹⁹F. L. Galeener, R. A. Barrio, E. Martinez, and R. J. Elliot, *Phys. Rev. Lett.* **53**, 2429 (1984).

²⁰E. I. Kamitsos and M. A. Karakassides, *Phys. Chem. Glasses* **30**, 19 (1989).

²¹Y. Deligiannakis, L. Astrakas, and G. Kordas, *Phys. Rev. B* **58**, 11420 (1998).

²²I. A. Shkrob, B. M. Tadjikov, S. D. Chemerisov, and A. D. Trifunac, *J. Chem. Phys.* **111**, 5124 (1999).

²³P. A. V. Johnson, A. C. Wright, and R. N. Sinclair, *J. Non-Cryst. Solids* **50**, 281 (1982).

²⁴R. L. Mozzi and B. E. Warren, *J. Appl. Crystallogr.* **3**, 251 (1970).

²⁵W. Soppe, C. van der Marel, and H. W. den Hartog, *J. Non-Cryst. Solids* **101**, 101 (1988).

²⁶W. Soppe, C. van der Marel, W. F. van Gunsteren, and H. W. den Hartog, *J. Non-Cryst. Solids* **103**, 201 (1988).

²⁷W. Soppe and H. W. den Hartog, *J. Non-Cryst. Solids* **108**, 260 (1989).

²⁸W. Soppe and H. W. den Hartog, *J. Phys. C* **21**, L689 (1988).

²⁹A. H. Verhoef and H. W. den Hartog, *Radiat. Eff. Defects Solids* **119-121**, 493 (1991).

³⁰A. H. Verhoef and H. W. den Hartog, *J. Non-Cryst. Solids* **146**, 267 (1992).

³¹H. Inoue, N. Aoki, and I. Yasui, *J. Am. Ceram. Soc.* **70**, 622 (1987).

³²R. Fernández-Perea, F. J. Bermejo, and E. Enciso, *Phys. Rev. B* **53**, 6215 (1996).

³³R. Fernández-Perea, F. J. Bermejo, and M. L. Senet, *Phys. Rev. B* **54**, 6039 (1996).

³⁴J. Swenson and L. Börjesson, *Phys. Rev. B* **55**, 11138 (1997).

³⁵M. Teter, in *Proceedings of the Second International Conference On Borate Glasses, Crystals, and Melts*, 1996, p. 407.

³⁶R. E. Youngman, J. Kieffer, J. D. Bass, and L. Duffrène, *J. Non-Cryst. Solids* **222**, 190 (1997).

³⁷A. Takada, C. R. A. Catlow, and G. D. Price, *J. Phys.: Condens. Matter* **7**, 8693 (1995).

³⁸F. H. Stillinger and C. W. David, *J. Chem. Phys.* **69**, 1473 (1978).

³⁹F. H. Stillinger, *J. Chem. Phys.* **71**, 1647 (1979).

⁴⁰F. H. Stillinger and D. Stillinger (private communication).

⁴¹F. H. Stillinger and C. W. David, *J. Chem. Phys.* **73**, 3384 (1980).

⁴²F. H. Stillinger and T. A. Weber, *Chem. Phys. Lett.* **79**, 259 (1981).

⁴³F. H. Stillinger and T. A. Weber, *J. Chem. Phys.* **76**, 4028 (1982).

⁴⁴T. A. Weber and F. H. Stillinger, *Phys. Rev. Lett.* **89**, 154 (1982).

⁴⁵T. A. Weber and F. H. Stillinger, *J. Chem. Phys.* **77**, 4150 (1982).

⁴⁶F. H. Stillinger, *Int. J. Quantum Chem.* **14**, 649 (1978).

⁴⁷F. H. Stillinger, T. A. Weber, and C. W. David, *J. Chem. Phys.* **76**, 3131 (1982).

- ⁴⁸ *Simulation of Liquids and Solids*, edited by G. Ciccotti, D. Frenkel, and I. R. McDonald (North-Holland, New York, 1987).
- ⁴⁹ F. H. Stillinger and T. A. Weber, *Phys. Rev. A* **28**, 2408 (1983).
- ⁵⁰ F. H. Stillinger, *Science* **267**, 1935 (1995).
- ⁵¹ F. H. Stillinger and T. A. Weber, *J. Chem. Phys.* **88**, 7791 (1988).
- ⁵² K. A. Peterson, *J. Chem. Phys.* **102**, 262 (1994).
- ⁵³ M. J. S. Dewar, C. Jie, and E. G. Zoebisch, *Organometallics* **7**, 513 (1998).
- ⁵⁴ M. J. S. Dewar and M. L. McKee, *J. Am. Chem. Soc.* **99**, 5231 (1977).
- ⁵⁵ F. Ramondo, L. Bencivenni, and C. Sadun, *J. Mol. Struct.* **209**, 101 (1990).
- ⁵⁶ M. T. Nguyen, P. Ruelle, and T.-K. Ha, *J. Mol. Struct.* **104**, 353 (1983).
- ⁵⁷ A. V. Nemukhin and F. Weinhold, *J. Chem. Phys.* **98**, 1329 (1993).
- ⁵⁸ W. H. Zachariasen, *Acta Crystallogr.* **16**, 385 (1954).
- ⁵⁹ T. T. Merzlyak, *J. Mol. Struct.* **344**, 171 (1995).
- ⁶⁰ A. S. Zyubin and S. A. Dembovsky, *Glass Phys. Chem.* **21**, 178 (1995).
- ⁶¹ L. Pauling, *The Nature of the Chemical Bond* (Cornell University Press, Ithaca, 1960).
- ⁶² A. C. Wright, N. M. Vedishcheva, and B. A. Shakhmatkin, *J. Non-Cryst. Solids* **192&193**, 92 (1995).